Nucleic Acids Research, 2017 **1**
doi: 10.1093/nar/gkx108

NAR Breakthrough Article

Molecular mechanism governing ratio-dependent transcription regulation in the *ccdAB* operon

Alexandra Vandervelde[1,2,†], Igor Drobnak[3,†], San Hadži[1,2,3], Yann G.-J. Sterckx[2,4], Thomas Welte[5], Henri De Greve[1,2], Daniel Charlier[6], Rouslan Efremov[1,2,*], Remy Loris[1,2,*] and Jurij Lah[3,*]

[1]Structural Biology Brussels, Department of Bioengineering Sciences, Vrije Universiteit Brussel, Pleinlaan 2, B-1050 Brussel, Belgium, [2]Center for Structural Biology, Vlaams Instituut voor Biotechnologie, B-1050 Brussel, Belgium, [3]Department of Physical Chemistry, Faculty of Chemistry and Chemical Technology, University of Ljubljana, Večna pot 113, 1000 Ljubljana, Slovenia, [4]Research Unit for Cellular and Molecular Immunology (CMIM), VUB, Pleinlaan 2, B-1050 Brussel, Belgium, [5]Dynamic Biosensors GmbH, Lochhamer Strasse 15, D-82152 Martinsried, Germany and [6]Research Group of Microbiology, Department of Bioengineering Sciences, Vrije Universiteit Brussel, Pleinlaan 2, B-1050 Brussel, Belgium

Received November 24, 2016; Revised January 25, 2017; Editorial Decision January 30, 2017; Accepted February 06, 2017

ABSTRACT

Bacteria can become transiently tolerant to several classes of antibiotics. This phenomenon known as persistence is regulated by small genetic elements called toxin–antitoxin modules with intricate yet often poorly understood self-regulatory features. Here, we describe the structures of molecular complexes and interactions that drive the transcription regulation of the *ccdAB* toxin–antitoxin module. Low specificity and affinity of the antitoxin $CcdA_2$ for individual binding sites on the operator are enhanced by the toxin $CcdB_2$, which bridges the $CcdA_2$ dimers. This results in a unique extended repressing complex that spirals around the operator and presents equally spaced DNA binding sites. The multivalency of binding sites induces a digital on-off switch for transcription, regulated by the toxin:antitoxin ratio. The ratio at which this switch occurs is modulated by non-specific interactions with the excess chromosomal DNA. Altogether, we present the molecular mechanisms underlying the ratio-dependent transcriptional regulation of the *ccdAB* operon.

INTRODUCTION

Persisters are non-growing, metabolically subdued cells within a bacterial population that are able to survive episodes of stress including antibiotic challenges (1,2). In contrast to resistance, which is an inherited trait that allows bacteria to grow in the presence of antibiotics, persistence is only temporary: when leaving the persistent state, bacterial cells again become sensitive and produce sensitive offspring (3). Persister cells are induced stochastically in a bacterial population, but their frequency depends on environmental conditions, and in particular the availability of nutrients. Persisters are rare in an exponentially growing culture and more abundant in the stationary phase (4). They are most important in biofilms and contribute to the difficulties in treating relapsing, chronic and biofilm-producing bacterial infections (5,6).

Toxin–antitoxin modules are found on the chromosomes and plasmids of most prokaryotes (7,8). The toxin generally targets the transcription or translation machinery of the cell, thereby inhibiting cell growth and potentially killing the cell. The antitoxin impairs the activity of the toxin, allowing cells to grow undisturbed. In type II toxin–antitoxin modules, this antitoxin is a protein that neutralizes the toxin by complex formation, but can be rapidly degraded by cellu-

*To whom correspondence should be addressed. Tel: +32 2 6291989; Fax: +32 2 6291963; Email: reloris@vub.ac.be
Correspondence may also be addressed to Jurij Lah. Tel: +386 1 4798 533; Fax: +386 1 2419 425; Email: Jurij.Lah@fkkt.uni-lj.si
Correspondence may also be addressed to Rouslan Efremov. Tel: +32 2 629 1025; Fax: +32 2 6291963; Email: rouslan.efremov@vub.ac.be
†These authors contributed equally to this work as the first authors.
Present addresses:
Alexandra Vandervelde, Department of Cellular and Molecular Medicine, KU Leuven, Leuven, 3000, Belgium.
Igor Drobnak, Department of Synthetic Biology and Immunology, National Institute of Chemistry, Hajdrihova 19, 1000 Ljubljana, Slovenia.

© The Author(s) 2017. Published by Oxford University Press on behalf of Nucleic Acids Research.
This is an Open Access article distributed under the terms of the Creative Commons Attribution License (http://creativecommons.org/licenses/by-nc/4.0/), which permits non-commercial re-use, distribution, and reproduction in any medium, provided the original work is properly cited. For commercial re-use, please contact journals.permissions@oup.com

lar proteases, releasing the active toxin. Different TA modules contribute cumulatively to persister frequency in *Escherichia coli* in non-stressed conditions during exponential growth (9). Activation of individual TA toxins has also been linked to specific stresses (10,11).

The *ccdAB* operon on the *E. coli* F plasmid was the first type II TA module to be discovered (12) and is well studied in terms of the gyrase poisoning activity of the toxin $CcdB_2$ (13–15) and the rejuvenation action of $CcdA_2$, i.e. its capacity to resolve poisoned $CcdB_2$-gyrase complexes (16–18). Initially only seen as a locus that couples plasmid replication to cell division (12), it is now also known to contribute to persistence (19). The antitoxin $CcdA_2$ can bind to DNA using its N-terminal ribbon–helix–helix domain (20) and is specifically degraded by Lon protease (21), while the interaction of $CcdB_2$ with DNA gyrase results in DNA cleavage and inhibits transcription by forming a roadblock for the passage of the RNA polymerases (15). There are two equivalent but partially overlapping binding sites for the $CcdA_2$ antitoxin on $CcdB_2$. The first $CcdA_2$ molecule binds the free $CcdB_2$ with a high affinity, but its presence obstructs the binding of the second $CcdA_2$, which subsequently binds with a low affinity. While only the high affinity binding is required for the rejuvenation of CcdB-poisoned gyrase, both binding sites play a role in the transcriptional regulation (18).

TA modules are precisely regulated, since their toxicity to the cell is determined by the molar toxin:antitoxin ratio. In many type II TA modules, this is accomplished by a negative autoregulation mechanism called conditional cooperativity. This mechanism has been investigated in detail at the molecular level for the *phd/doc* and the *relBE* TA modules (22–24). In general, the antitoxin binds the operator DNA, which overlaps with the promoter, and the toxin can either function as a co-repressor or a de-repressor for the antitoxin, depending on the amounts of toxin and antitoxin present in the cell (22,25).

Regulation of the F-plasmid *ccdAB* operon also involves conditional cooperativity (26), but the underlying mechanism is not understood at the molecular level. An intriguing open question is the role of the unusually long (113 bp) *ccdAB* promoter/operator region, containing eight putative antitoxin binding sites (27,28). It has been proposed that avidity plays a role in the transcriptional regulation of this operon (18,29). Avidity, also referred to as functional affinity, describes the cumulative strength of multiple non-covalent binding interactions (30). The concept of avidity was coined in the context of the polyvalency of antibodies, where multiple binding sites were observed to enhance antigen binding (31,32). Avidity effects have since been observed in many biochemical contexts including the interactions between carbohydrates and lectins (33,34) and pattern recognition by collectins in the innate immune system (35,36). Such avidity effects, induced by the bridging of antitoxins by toxins, cause an increase in the apparent affinity of the repressing complex for the operator DNA.

Here, we investigate the biochemical basis of the avidity in the transcriptional regulation of the *ccdAB* toxin–antitoxin module and present structures of complexes involved in this regulation. At low toxin:antitoxin ratios, the operator is repressed by a chain of alternating $CcdA_2$ antitoxins and $CcdB_2$ toxins spiraling around the DNA. As the toxin:antitoxin ratio increases, the repression is relieved because of the preferential formation of the V-shaped non-repressing $CcdB_2$-$CcdA_2$-$CcdB_2$ heterohexamer. The forces that drive this ratio-dependent switching were identified by a global thermodynamic analysis. Together, these analyses put forward the molecular mechanisms underlying the avidity effects in the conditional cooperativity regulation of the *ccdAB* toxin–antitoxin module.

MATERIALS AND METHODS

Protein production

The GyrA fragments GyrA14 and GyrA59 were purified according to the protocol described for GyrA14 by Dao-Thi *et al.* (37).

The antitoxin $CcdA_2$ was purified using a protocol modified from Van Melderen *et al.* (38). An overnight preculture of *E. coli* CSH50 *lon*::Tn10 (pULB2709) (16), grown at 37°C in Terrific Broth medium supplemented with ampicillin (100 μg/ml), was diluted 30 times in Terrific Broth and grown at 37°C. When the culture reached an OD_{600} of 0.6 to 0.8, it was induced by adding isopropyl β-D-thiogalactopyranoside at a final concentration of 1 mM. After overnight incubation at 28°C, the cells were harvested and resuspended in lysis buffer (50 mM Tris-HCl pH 8, 0.1 mM ethylenediaminetetraacetic acid (EDTA), 2% glycerol, 0.1 mg/ml 4-(2-aminoethyl) benzenesulfonyl fluoride hydrochloride, 1 μg/ml leupeptine).

The cells were lysed by sonication and the cell debris was removed by centrifugation. Next, the protein was precipitated with 40% saturated ammonium sulfate. After centrifugation, the pellet was resuspended in and dialyzed against 20 mM Tris pH 8 (buffer A). It was then applied to a Source 30Q anion exchange column equilibrated with buffer A. Proteins were eluted using a linear gradient of 20 mM Tris pH 8, 1 M NaCl (buffer B). The fractions containing $CcdA_2$ were pooled, concentrated and loaded on a Superdex 200 16/90 column (GE Healthcare), equilibrated with buffer B. After gel filtration, the relevant fractions were pooled, dialyzed against distilled water, flash-frozen in liquid nitrogen and lyophilized overnight. The protein was finally checked for purity using mass spectrometry and the quality of the preparation was verified using SAXS on an in-house Rigaku BioSAXS 2000.

The toxin $CcdB_2$ was available from previous studies (18).

Small angle X-ray scattering

Data were collected at the SWING beamline, SOLEIL synchrotron (Gif-Sur-Yvette, France) in high pressure (or high performance) liquid chromatography mode (39). The $CcdB_2$-$CcdA_2$-$CcdB_2$ complex was prepared at a concentration of 7 mg/ml in 10 mM Tris pH 7.3, 50 mM NaCl by slowly titrating $CcdA_2$ into an excess of $CcdB_2$. The sample was injected onto a Shodex KW402.5-4F column, which had been pre-equilibrated with running buffer (10 mM Tris pH7.3, 50 mM NaCl) for at least one column volume. The flow rate was 0.2 ml/min and data were collected with an exposure time of 750 ms and a dead time of 750 ms. Buffer data were collected at the beginning of the chromatogram

and sample data were collected in the peak area. Data reduction was performed on-line using the FOXTROT software (SWING), while buffer subtraction and data averaging was performed using DATASW (40). Further analysis of the resulting scattering curve was performed using the ATSAS package (41). The indirect transform program GNOM was used to calculate the particle distance distribution function p(r) (42). Ten *ab initio* shape reconstructions were generated using DAMMIF (43) and averaged using DAMAVER (44). The shown *ab initio* envelope corresponds to the damfilt model.

Based on the N-terminal region of the solution structure of $CcdA_2$ (20), encompassing residues 1 until 39 (PDB: 2ADL) and the crystal structure of the complex of $CcdB_2$ with the C-terminal part of CcdA, $CcdA^{37\text{-}72}$ (PDB: 3HPW), a model for the $CcdB_2$-$CcdA_2$-$CcdB_2$ complex (model A) was built, assuming that the $CcdA_2$ α-helices from the two models will extend into one continuous α-helix. The Allosmod-FOXS server (45,46) was then used to generate 100 structures similar to the input structure. The theoretical scattering curve of these models was then compared to the experimental data using CRYSOL (47).

Electron microscopy sample preparation

A 1000 bp long DNA fragment containing the *ccdAB* promoter/operator region was PCR amplified with primers EM1000centrFwd (5′-AATTGTGATGCTTCTAAAATT ACTA-3′) and EM1000centrRev (5′-GGTTAATGGCG TTTTTGATGT-3′) from the F' plasmid present in *E. coli* CSH100 (48). The resulting PCR fragment was then purified and concentrated using the Promega Wizard SV Gel and PCR clean-up system.

All binding reactions were performed in 30 mM Tris HCl pH 7.5, 200 mM NaCl, 0.5 mM EDTA. For the thin filaments, the binding reactions occurred at 20°C. DNA was first incubated with $CcdA_2$ for 15 min. After adding $CcdB_2$, the resulting mixture with final concentrations of 15 nM for the DNA duplex and 2.5 μM for $CcdA_2$ and $CcdB_2$ was incubated for another 15 min before preparing the EM sample. Thick filaments were prepared at 4°C. Again, the DNA was first incubated for 15 min with $CcdA_2$ alone. After adding $CcdB_2$, the mixture with final concentrations of 15 nM for the DNA duplex and 10 μM for $CcdA_2$ and $CcdB_2$ was incubated overnight at 4°C.

Negative stain samples were prepared by applying three microliters of $CcdA_2$-$CcdB_2$-DNA mixture supplemented with 5 mM $MgAc_2$ on a freshly glow-discharged carbon-coated grid for 5 min after which the grid was washed with 5 mM $MgAc_2$ and adsorbed protein stained with 1% uranyl formate.

Samples for cryogenic electron microscopy (cryo-EM) were prepared by applying 2 μl of $CcdA_2$-$CcdB_2$-DNA on a freshly glow-discharged holey carbon grid (Quantifoil, Germany) with additional 2 nm thick carbon layer. The sample was blotted manually for 2 s and vitrified by plunging in liquid ethane.

EM data collection and image processing

All EM images were collected on a JEOL JEM-1400 electron microscope equipped with LaB_6 cathode and operated at 120 kV. Images were recorded on 4096 × 4096 pixels CMOS TemCam-F416 (TVIPS) camera. The negative stain data were collected at nominal microscope magnification of 50 000 and corresponding pixel size at the detector of 2.29 Å. The defocus was in the range between 1.2 and 3.0 μm. For the sample prepared at high and low CcdA-CcdB/DNA ratio 382 and 358 micrographs were collected, respectively. A total of 77 cryo-EM images were collected at nominal magnification of 40 000, corresponding pixel size of 2.87 Å and defocus range of 1.6 to 3.0 Å. For image processing, helices were boxed in e2helixboxer (49), 2D classes and 3D reconstruction by IHRSR procedure were performed in SPARX (50). The hand of the thick helices was determined by the tilt method (51) (see Supplementary Text: Electron Microscopy).

Model building

First, a model for the 113 bp *ccdAB* promoter/operator DNA was generated using the 3D-DART server (52). The helical axis of the model was aligned to the axis of the EM map. To correctly place the first $CcdA_2$ dimer on the central 5′-GTATAC-3′ binding site, the solution structure of $CcdA_2$ in complex with this binding site (PDB 2H3C) (20) was first aligned with the DNA. Then, the antitoxin $CcdA_2$ from the $CcdB_2$-$CcdA_2$-$CcdB_2$ heterohexamer refined to the experimental SAXS curve was aligned to this $CcdA_2$ dimer. The helical symmetry of the 3D reconstruction was then applied to $CcdA_2$ to generate the adjacent antitoxin on the DNA. To connect the two antitoxins, the crystal structure of $CcdB_2$ in complex with two CcdA peptides was used (PDB 3G7Z) (18). The CcdA α helices in the latter structure were aligned with the $CcdA_2$ α helices from the $CcdB_2$-$CcdA_2$-$CcdB_2$ heterohexamer. The minimal helical unit for the protein chain finally consists of residues 1–40 of the two central CcdA antitoxin monomers from the $CcdB_2$-$CcdA_2$-$CcdB_2$ heterohexamer, combined with residues 41–72 of the two CcdA peptides and the $CcdB_2$ toxin from structure 3G7Z. The geometry of this minimal helical unit was then optimized using Coot (53). The helical symmetry of the 3D reconstruction was applied to this minimal helical unit to obtain a continuous model consisting of alternating $CcdA_2$ and $CcdB_2$ dimers. For the thick helices, two additional strands were generated by translating the minimal helical unit by 67.2 Å and 134.4 Å along the helical axis, and again applying the helical symmetry. Model building was performed in UCSF Chimera (54).

Electrophoretic mobility shift assays

Electrophoretic mobility shift assays (EMSAs) were performed on 5′-^{32}P single-end-labeled oligonucleotide duplexes (Table 1). These were prepared by labeling one oligonucleotide of each duplex with γ-^{32}P-ATP (Perkin Elmer) and T4 polynucleotide kinase (Fermentas). The duplexes were then annealed by incubating both oligonucleotides at 80°C during 10 min and cooling slowly overnight in a water bath. The labeled duplexes were purified by electrophoresis on a native 8% polyacrylamide gel.

All binding reactions were performed at 20°C in 30 mM Tris-HCl pH 7.5, 200 mM NaCl, 0.5 mM EDTA, 150 μg/ml

bovine serum albumin, in the presence of 0.25 μg/lane sonicated salmon sperm DNA. First, $CcdA_2$ and labeled DNA (7500 cpm) were incubated together for 15 min in a total volume of 10 μl. After adding $CcdB_2$, the resulting mixture of 15 μl was incubated again for 15 min. The samples were then mixed with 3 μl loading dye (25% ficoll, 0.1% xylene cyanol, 0.1% bromophenol blue) and loaded on a native 8% (for the 42 bp fragments) or 6% (for the full length operator) polyacrylamide gel prepared with TBE buffer (89 mM Tris-HCl, 89 mM boric acid, 2.5 mM EDTA). The electrophoresis was then performed at 12 V/cm until the sample had penetrated into the gel, and at 8 V/cm during 3 h, using TBE as the running buffer. An X-ray sensitive film was exposed to the gel overnight and then developed. The further data analysis is described in the supplementary text.

SwitchSENSE

All experiments were carried out on a switchSENSE analyzer DRX 2400 (Dynamic Biosensors GmbH, Munich, Germany). The switchSENSE technology evaluates the electrically actuated dynamic movement of DNA nanolevers that are immobilized on gold microelectrodes. Briefly, the DNA nanolevers which are modified with a fluorescent dye at the distal end are driven to oscillate on the surface of microelectrodes by alternating electric fields and their orientation-switching is analyzed by time-resolved single photon counting as described by Langer *et al.* (55). The nucleotide sequence of the DNA nanolevers was designed specifically to include the target six base-pair DNA sequence. Upon binding of an interaction partner to the DNA its movement is slowed down due to the increased hydrodynamic drag, which can be evaluated by a change in the Dynamic Response.

The on-chip exchange of DNA sequences was carried out by use of EXMAS system (exchangeable modular anchor sequences, Dynamic Biosensors GmbH, Munich, Germany), which is based on the specific hybridization of complementary overlapping strands.

Isothermal titration calorimetry (ITC)

Purified, lyophilized proteins were dissolved in water, then dialyzed against phosphate buffer (10 mM Na_2HPO_3, 10 mM NaH_2PO_3, 150 mM NaCl, 1 mM EDTA, pH 7.2). After dialysis, their concentrations (expressed as dimer equivalents for $CcdA_2$, $CcdB_2$ and the gyrase fragments) were determined by measuring absorbance of light at 280 nm (56). DNA oligonucleotides were similarly dissolved in water, complementary strands were mixed and annealed by heating to 90°C and cooling down to room temperature at 1°C/min. DNA concentration was determined by measuring absorbance at 260 nm (57) and correct 1:1 annealing was confirmed by a job plot (58). All solutions were filtered through a 0.45 μm membrane and degassed prior to titration. Titration was performed using the VP-ITC instrument (MicroCal, now part of Malvern Instruments, UK). Typical concentrations used were 1–3 μM protein in the cell and a 5- to 20-fold higher concentration of the titrant in the syringe. Typical injection volumes were 5–10 μl. The thermodynamic model of the *ccdAB* system (described below) was fitted to experimental data from all titrations simultaneously to yield the set of thermodynamic parameters that best describes the interactions between different binding partners at different temperatures.

Because of experimental limitations, not all binding reactions in the system could be measured directly. For instance, $CcdA_2$ and $CcdB_2$ tend to form insoluble aggregates at molar ratios around 1:1, presumably by forming long chains of alternating dimers ($\ldots CcdA_2{:}CcdB_2{:}CcdA_2{:}CcdB_2\ldots$) (28). To work around that, most titrations were performed using a truncated version of CcdA, $CcdA_C$ (Supplementary Figure S1A–D). $CcdA_C$, also known as $CcdA^{37-72}$, is comprised of the entire C-terminal domain that binds to $CcdB_2$, but lacks the dimerization domain so it cannot form chains of alternating dimers (18,59). To study DNA binding, on the other hand, full-length $CcdA_2$ was used; in this case DNA was always present in sufficient amounts to take up any $CcdA_2{:}CcdB_2$ 1:1 complexes before they could aggregate. Another limitation is that affinity of the first $CcdA_2$ dimer for $CcdB_2$ cannot be accurately assessed from direct titrations because the very strong binding makes isothermal titration calorimetry (ITC) titration curves very sharp and compatible with a wide range of binding affinities during fitting (Supplementary Figure S1A). This was overcome by first titrating $CcdB_2$ with a truncated gyrase dimer, $GyrA14_2$, (Supplementary Figure S1B) and then titrating the $CcdB_2{:}GyrA14_2$ complex with $CcdA_C$ (Supplementary Figure S1C). In the second titration, $CcdA_C$ needs to displace $GyrA14_2$ before it can bind to $CcdB_2$, so the free energy of this process gives us the difference between $CcdA_C{:}CcdB_2$ binding and $CcdB_2{:}GyrA14_2$ binding, from which the $CcdA_C{:}CcdB_2$ affinity can be calculated. Similarly, the affinity of $CcdB_2$ for the poorly soluble full-length gyrase ($GyrA59_2$) was obtained by titrating the $CcdB_2{:}GyrA59_2$ complex with $CcdA_C$ and comparing that to the separately determined affinity of $CcdA_C$ for $CcdB_2$.

The thermodynamic parameters of all these processes were determined by fitting a thermodynamic model to all data simultaneously. The global fitting methodology has already been described in detail (59). It is important to note that a global fit, i.e. one that optimizes every model parameter against all available data, was necessary to make sure all model parameters are consistent with each other and with all the data from different titrations (60).

Global thermodynamic model

The thermodynamics of the *ccdAB* system were described in terms of the following reaction equilibria:

$$2\,(B_2 : G_2) + A_2 \overset{K_H^2 K_{G59}^{-2}}{\rightleftharpoons} 2G_2 + (B_2 : A_2 : B_2)$$

$$(B_2 : A_2 : B_2) + A_2 \overset{K_L}{\rightleftharpoons} (B_2 : A_2 : B_2 : A_2) \overset{K_L^{-1}}{\rightleftharpoons} 2\,(A_2 : B_2)$$

$$(A_2 : B_2) + A_2 \overset{K_L}{\rightleftharpoons} (A_2 : B_2 : A_2)$$

$$A_2 + B_2 + \tfrac{1}{3}D_2 \overset{K_D}{\rightleftharpoons} \tfrac{1}{3}D_2A_6B_6$$

$$\tfrac{1}{2}A_2 \overset{K_U}{\rightleftharpoons} A_U.$$

A, B, G and D represent CcdA, CcdB, GyrA and promoter DNA (central 3 binding sites), respectively. The different K_i

Table 1. Oligonucleotides used in this work. Underlined sequences indicate the three central binding sites

Name	Sequence
Ccd1	5′-ACGTACCTTCCTCTTTATGTATACCCGGCAGGACTGGAAATA-3′ 3′-TGCATGGAAGGAGAAATACATATGGGCCGTCCTGACCTTTAT-5′
Ccd2	5′-ACGTACCTTCATATATACTGATATGTATACCCGCTGGAAATA-3′ 3′-TGCATGGAAGTATATATGACTATACATATGGGCGACCTTTAT-5′
Ccd3	5′-ACGTGCGGTATAAGAATATATACTGATATGTATACCCGAATA-3′ 3′-TGCACGCCATATTCTTATATATGACTATACATATGGGCTTAT-5′
Random	5′-TGCCCAAGTGATGCTAAACAAGACTTAGCTGGTTCCTGTGTT-3′ 3′-ACGGGTTCACTACGATTTGTTCTGAATCGACCAAGGACACAA-5′
Full length	5′-CAGTATGCGTATTTGCGCGCTGATTTTTGCGGTATAAGAATATATACT 3′-GTCATACGCATAAACGCGCGACTAAAAACGCCATATTCTTATATATGA GATATGTATACCCGAAGTATGTCAAAAAGAGGTGTGCTATGAAGCAGCGTA CTATACATATGGGCTTCATACAGTTTTTCTCCACACGATACTTCGTCGCAT TTACAGTGACAGTT-3′ AATGTCACTGTCAA-5′
CcdITC	5′-GCGGTATAAGAATATATACTGATATGTATACCC-3′ 3′-CGCCATATTCTTATATATGACTATACATATGGG-5′

are the equilibrium constants describing the high-affinity binding of the first $CcdA_2$ antitoxin to $CcdB_2$ (K_H), the low-affinity binding of the second $CcdA_2$ antitoxin to the same $CcdB_2$ (K_L), the binding of $CcdB_2$ to $GyrA_2$ (K_G), the binding of each $CcdA_2$:$CcdB_2$ complex to operator DNA (K_D) and the temperature-induced denaturation of $CcdA_2$ (K_U). The latter reaction was studied to verify that the unfolding of $CcdA_2$ does not play a significant role in the regulation of *ccdAB* (see Supplementary Data for details). For each reaction in the above scheme, the equilibrium equation states that the equilibrium constant must equal the ratio between the equilibrium concentrations of products and reactants:

$$K_i = \frac{\prod_{\text{products p}} [p]^{\nu_{p,\,i}}}{\prod_{\text{reactants r}} [r]^{\nu_{r,\,i}}},$$

where [p] and [r] are the equilibrium concentrations of products and reactants, respectively, while $\nu_{p,i}$ and $\nu_{r,i}$ are their stoichiometric coefficients in reaction i. The six equilibrium reactions, combined with the conservation of mass for each of the four basic building blocks (CcdA, CcdB, GyrA and DNA), define a system of non-linear equations that can be solved to yield the equilibrium composition of the entire system. Thus the system composition is completely defined by the constants K_i and total concentrations of each building block c_j.

c_j were determined by measuring the concentrations of each solution going into an experiment, while K_i were calculated from the standard Gibbs free energy of the reaction, $\Delta G^\circ_i = -RT \ln K_i$, where R is the gas constant and T is the absolute temperature. ΔG°_i changes with temperature according to the Gibbs–Helmholtz relation,

$$\frac{d\left(\Delta G^\circ_i / T\right)}{dT} = -\frac{\Delta H^\circ_i}{T^2},$$

and the Kirchhoff relation,

$$\frac{d\Delta H^\circ_i}{dT} = \Delta c^\circ_{(p,i)},$$

where ΔH°_i and $\Delta c^\circ_{p,i}$ are the standard enthalpy and heat capacity of reaction i. With $\Delta c^\circ_{p,i}$ assumed to be constant across the range of experimental temperatures, these three equations allowed us to calculate K_i at any temperature using three parameters: $\Delta G^\circ_i(25^\circ C)$, $\Delta H^\circ_i(25^\circ C)$ and $\Delta c^\circ_{p,i}$. From K_i and c_j we calculated the equilibrium concentrations of all molecular species using the Newton method with adaptive step size (61). By calculating the composition of the experimental system at each point during an experimental run (either ITC, DSC or CD temperature denaturation scans), we were able to calculate the model-based value of the experimental signal, dependent only on the parameters $\Delta G^\circ_i(25^\circ C)$, $\Delta H^\circ_i(25^\circ C)$ and $\Delta c^\circ_{p,i}$. These parameters were adjusted to produce the best fit of model-based signal to experimentally measured values by minimizing χ^2 using the Nelder–Mead optimization algorithm with simulated annealing (61).

Simulations of the *ccdAB* regulation

All simulations are based on the experimentally determined equilibrium constants obtained from the global analysis of the ITC data (Supplementary Table S1). For a given model, a set of non-linear equations was defined by the equilibrium constants and total concentrations of the building blocks c_j and solved using the trust-region dogleg algorithm (62) as implemented in the fsolve function from the scipy.optimize package (based on MINPACK1) (63). Total concentrations of toxin and antitoxin dimers were in 0–1 μM range, while fixed total concentrations of operator (1 nM), gyrase (100 nM) and non-specific DNA (42 μM) were assumed.

Two models were used in the simulations of the *ccdAB* system behavior: the simple and the extended model. In the absence of non-specific DNA, both models provide very similar results (Supplementary Figure S2A and B), therefore the computationally less demanding simple model was used in such cases. Simple model was introduced in the previous section (see Global Thermodynamic Model) and considers formation of only one kind of alternating $(CcdA_2\text{-}CcdB_2)_n$ complex, where n is the number of the binding sites on the operator. For three binding sites, such model is in complete agreement with the experimental data, therefore it was used to calculate the phase space. To study the effects of the multiplicity of antitoxin binding sites in the system, we varied the number of binding sites assuming the additivity of the corresponding free energies (Supplementary Figure S3A). Influence of affinity constants variations on the

system behavior were studied with n = 8 using the simple model (Supplementary Figure S3B–E).

The extended model is superior in describing the system when non-specific DNA is included (Supplementary Figure S2C and D). The extended model considers all possible chain complexes $(CcdA_2)_n$:$(CcdB_2)_{n-1}$, $(CcdA_2)_n$:$(CcdB_2)_n$ and $(CcdA_2)_n$:$(CcdB_2)_{n+1}$ where n runs from 1 to 8. These complexes can bind to the operator and to the non-specific DNA. Here, we assume that non-specific DNA is represented as a group of equivalent binding sites (64). Since the extended model assumes the presence of over 200 different species, the calculation of the whole phase diagram proved to be computationally too demanding. We performed calculations only on the 1D sections of the phase diagram.

RESULTS

The non-repressing $CcdB_2$-$CcdA_2$-$CcdB_2$ heterohexamer is a V-shaped complex

Repression of the *ccdAB* operon is known to be relieved at high toxin:antitoxin ratios, when a soluble heterohexameric $CcdB_2$-$CcdA_2$-$CcdB_2$ species is formed (26). To understand the molecular mechanism of derepression, we first investigated the structure of this non-repressing complex using HPLC-SAXS (Figure 1A, Supplementary Figure S4A). Molecular weight calculations based on the absolute I(0), DATMOW and the excluded volume in *ab initio* modeling correspond well with the expected molecular weight for a complex with a $CcdA_2$-$CcdB_4$ stoichiometry (Supplementary Table S2).

An initial model for this complex was built by combining the solution structure of the N-terminal DNA binding domain of $CcdA_2$ (20) and the crystal structure of the complex of $CcdB_2$ with the C-terminal peptide of CcdA (18). After refinement with AllosMod-FoXS (45), the theoretical scattering curve from this model fits the experimental scattering curve with a χ^2 of 2.5 (Figure 1A and B). Furthermore, the refined model fits well into an *ab initio* envelope generated using DAMMIF (Figure 1B). Interestingly, the dimensionless Kratky plot suggests a limited degree of dynamics in the $CcdB_2$-$CcdA_2$-$CcdB_2$ hexamer (Supplementary Figure S4B).

$CcdA_2$-$CcdB_2$ complexes assemble on the DNA into two types of helical structures

To elucidate the structure of the *ccdAB* repressor complex, we visualized $CcdA_2$ and $CcdB_2$ bound to a 1000 bp DNA fragment of the F plasmid encompassing the 113 bp *ccdAB* operator using negative stain transmission electron microscopy. We found that depending on the protein concentration, two types of structures are formed: short, relatively thin spirals at lower $CcdA_2$ and $CcdB_2$ concentrations, and longer, thick, continuous filaments at higher protein concentrations (Figure 2). These structures are not limited to the operator region, but extend over the length of the entire DNA fragments.

The thin filaments have a diameter of ~90 Å and are typically 100–250 nm long, while the thick helices have a diameter of ~130 Å and are often more than 1 μm long. This suggests that either the protein chain extends further than

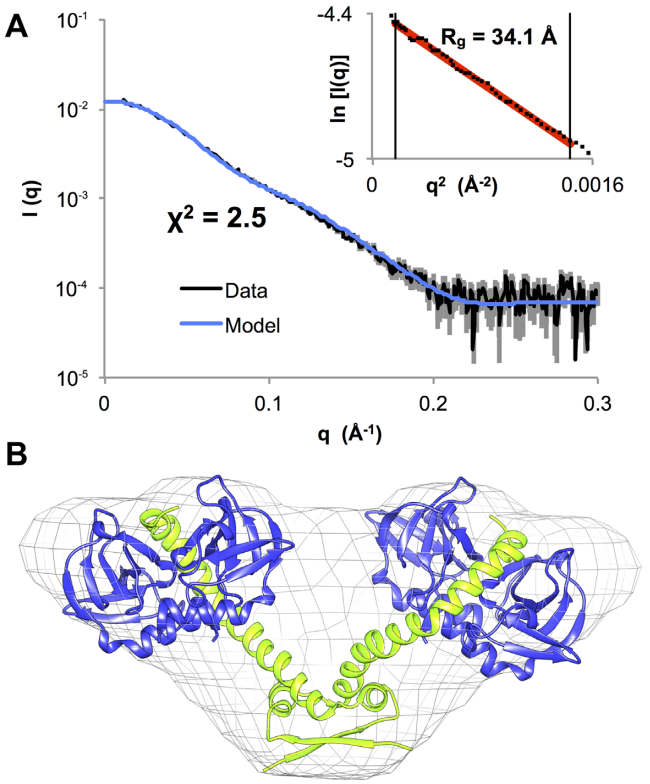

Figure 1. The solution structure of the $CcdB_2$-$CcdA_2$-$CcdB_2$ non-repressing complex is a V-shaped heterohexamer. (**A**) Experimental scattering curve for the $CcdB_2$-$CcdA_2$-$CcdB_2$ heterohexamer (black) and fit of the theoretical scattering curve (blue) calculated based on the model shown in panel B. The Guinier plot is shown in the inset. (**B**) Structural model for the $CcdB_2$-$CcdA_2$-$CcdB_2$ heterohexamer fitted in the *ab initio* envelope generated based on the experimental scattering curve shown in panel A. The $CcdA_2$ antitoxin dimer is shown in green and the $CcdB_2$ toxin dimers are shown in blue.

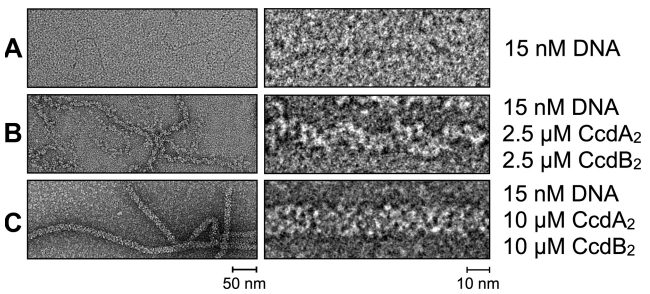

Figure 2. Negative stain electron microscopy shows the different complexes $CcdA_2$ and $CcdB_2$ form with a 1000 bp DNA fragment containing the 113 bp *ccdAB* operator region. (**A**) DNA without proteins. (**B**) DNA with $CcdA_2$ and $CcdB_2$ at concentrations of 2.5 μM. (**C**) DNA with $CcdA_2$ and $CcdB_2$ at concentrations of 10 μM.

the length of the DNA (~340 nm), or it concatenates several individual pieces of the DNA duplex. The high protein concentrations at which the thick filaments are observed (with an excess of protein over binding sites on the DNA), combined with DNase footprinting experiments showing only a limited protection of the operator in the presence of $CcdA_2$ and $CcdB_2$ (28), indicate that the thin filaments closer reflect the arrangement of proteins and DNA in the repress-

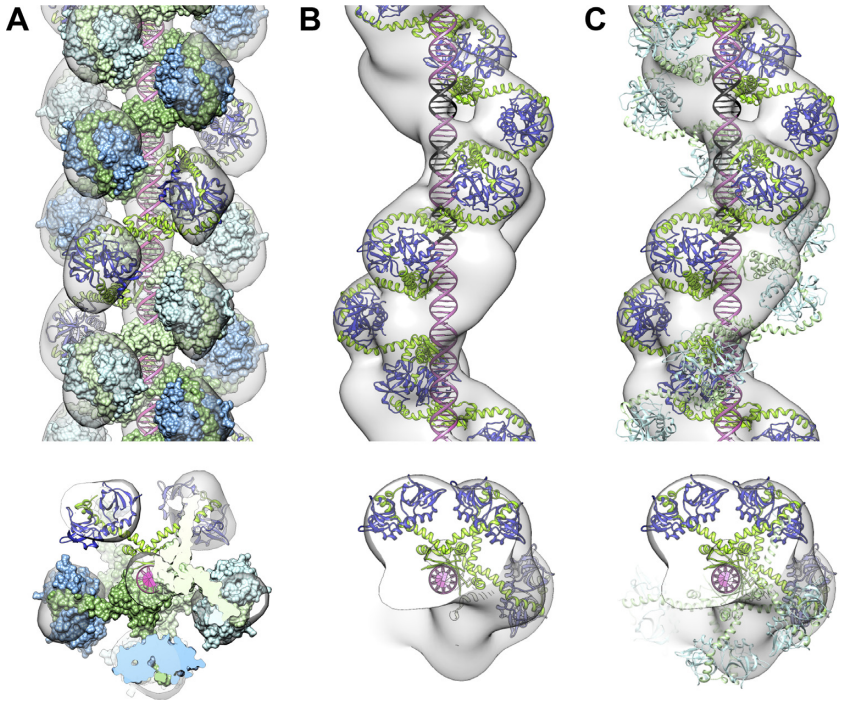

Figure 3. The structures of $CcdA_2$-$CcdB_2$-DNA helical assemblies consist of chains of DNA-bound antitoxins bridged by toxins. (**A**) Front view and top view of the cryo-EM density map and structural model for the thick filaments, corresponding to three strands of alternating $CcdA_2$ and $CcdB_2$ dimers spiraling around the DNA. The three-start right-handed helices have a pitch of 208 Å, a corresponding unit helical rise of 41.6 Å and a helical twist of 72°. (**B** and **C**) Front view and top view of the negative stain EM density map and structural model for the thin filaments. The panels show the EM density map for the data set with a pitch of 215 Å, a unit helical rise of 38.4 Å and a unit twist of 64.3°. (**B**) The DNA is bound by one strand of alternating $CcdA_2$ and $CcdB_2$ dimers. (**C**) The DNA is bound by two strands of alternating $CcdA_2$ and $CcdB_2$ dimers. The second strand of alternating dimers (shown in lighter colors) is only partially occupied in the negative stain-EM ensemble. The three main binding sites for $CcdA_2$ on the operator are indicated in black.

ing complex. However, while both helical assemblies appear heterogeneous, the thick helices are more homogeneous and contain longer straight sections than the thin ones, making them more suitable for cryo-EM. Therefore, a pseudo-atomic model for the thick filaments was obtained first to aid the structure determination of the actual operator complex.

A triple helix of alternating $CcdA_2$ and $CcdB_2$ dimers saturates the operator

The 3D structure of the thick filaments was studied using negative stain and cryo-EM (Supplementary Figure S5A–F). The 3D helical reconstruction, calculated to a resolution between 20 and 25 Å, shows that the filaments are formed by right-handed triple helices (Supplementary Figure S6A and B). Each helical strand contains five helical units per turn. High density at the helical axis of the cryo-EM reconstruction is consistent with double stranded DNA being present in the center of this triple protein helix (Supplementary Figure S6A - Cryo).

We used the SAXS structure of the $CcdB_2$-$CcdA_2$-$CcdB_2$ hexamer described above to fit a molecular model in the EM reconstruction. This EM reconstruction is consistent with three continuous chains of alternating $CcdA_2$ and $CcdB_2$ dimers spiraling around the DNA (Figure 3A). The build-up of this complex is shown in Supplementary Figure S7. In this model, the antitoxins $CcdA_2$ are bound in the major groove of the DNA as in the previously published $CcdA_2$-DNA NMR ensemble (20) while $CcdB_2$ toxins line the outer surface of the triple helix. These $CcdB_2$ dimers do not form direct contacts with the DNA or each other, neither within protein strands nor between protein strands. Therefore, the binding of $CcdA_2$–$CcdB_2$ complexes to DNA is likely independent for different strands. The spacing of the $CcdA_2$ molecules on the DNA mirrors the ∼12 bp spacing of the imperfect palindromes on the 113 bp operator sequence. In the triple helix arrangement, $CcdA_2$ antitoxins are stacked next to each other in the major groove of the B-form DNA, which they fill completely (Supplementary Figure S8).

It is also noteworthy that this model can explain the concatenation of several DNA fragments: each of the three protein strands surrounding the DNA will either end with a $CcdA_2$ dimer or with a $CcdB_2$ dimer. When two such protein-bound DNA fragments meet, these compatible ends will bridge the two DNA fragments resulting in the observed long assembly of thick filaments.

Structural properties of the repressing complex

Negative stain EM images of the thin filaments indicate a significant heterogeneity in the helical parameters. Reference-free 2D class averages display differences in the pitch of the helices ranging from ca. 190 Å to 340 Å (Supplementary Figure S5G and Supplementary text: Electron Microscopy), with the refined pitch of the most populated class (203–230 Å) close to the pitch of the thick helices.

Three-dimensional reconstructions from the three most

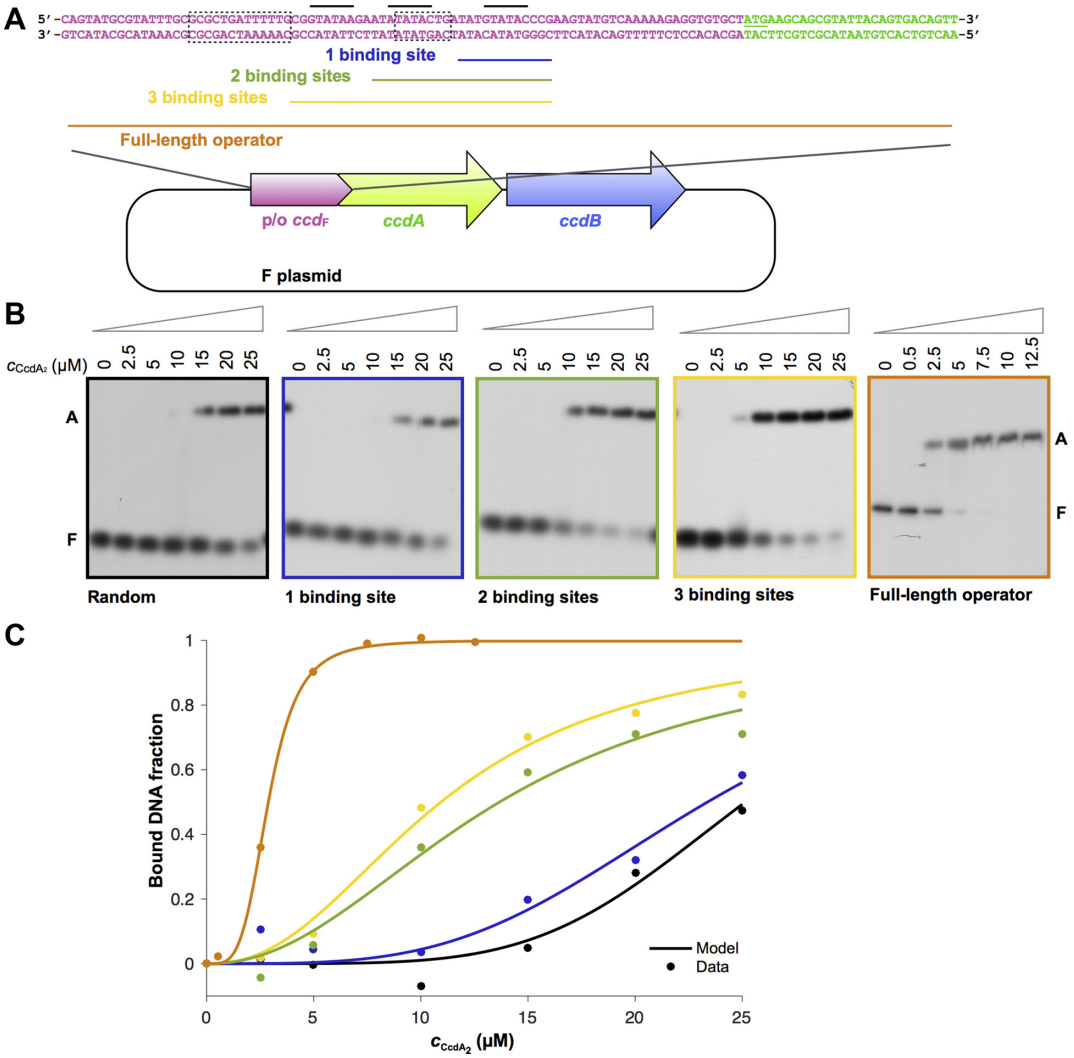

Figure 4. Antitoxin $CcdA_2$ has a low affinity and sequence specificity for *ccdAB* operator fragments. (**A**) The promoter/operator region of the *ccdAB* operon on the F plasmid of *E. coli*. The promoter/operator is shown in pink, the *ccdA* gene in green and the *ccdB* gene in blue. The three central binding sites of the operator are indicated with a black line, the −10 and −35 promoter elements (12) with a dotted box, and the parts of the *ccdAB* promoter/operator embedded in the DNA duplexes for EMSA experiments are indicated with a colored line. (**B**) Autoradiographs of EMSA analyses of $CcdA_2$ binding to 42 bp duplexes of random DNA, to 42 bp duplexes with fragments of the *ccdAB* operator (1–3 binding sites) embedded in random DNA and to the 113 bp full length operator. The concentration of $CcdA_2$ is indicated above the lanes. The positions of free DNA (marked as F) and DNA bound by $CcdA_2$ (marked as A) are indicated next to the lanes. (**C**) Binding profiles of the EMSAs shown in panel B.

populated classes, calculated to a resolution between 23 and 31 Å (Supplementary Figure S6C), show that these helices are formed by a main strand of density that is similar to the strands observed in the 3D reconstructions of the thick helices. The heterogeneity of the helical parameters originates from differences in the unit helical twist angle (∼15° for pitches between 180 and 258 Å) rather than from differences in the helical rise (Supplementary Table S3) and is consistent with the limited flexibility observed for the $CcdB_2$-$CcdA_2$-$CcdB_2$ hexamer.

The $CcdA_2$-$CcdB_2$-DNA complexes that are observed as thin filaments thus constitute in a first approximation a substructure of the thick filaments (assuming DNA is in the center), with one strand of $CcdA_2$-$CcdB_2$ repeats spiraling along the DNA. Therefore, a single chain of alternating $CcdA_2$-$CcdB_2$ repeats was built into the 3D reconstructions for the thin helices, as described above for the thick helices (Figure 3B). Analysis of this helical structure shows that a single strand of alternating $CcdA_2$ and $CcdB_2$ dimers is sufficient to bind to all the eight imperfect palindromes (this is shown in Figure 3B for the three central binding sites) and is consistent with the DNase I footprinting results (27,28). Therefore, we expect that a single stranded assembly is sufficient to form the repressing complex assembling *in vivo*.

Nevertheless, additional density unexplained by the single strand structural model was present in the 3D reconstruction for the thin filaments (Figure 3B, Supplementary Figure S9). We interpret this additional density as a second strand of toxin and antitoxin dimers with partial occupancy. In some of the micrographs for the thin helices, a second strand of features can unambiguously be observed (e.g. Figure 2B, right). This second strand was included in the model

for the most populated class of thin helices by translating and rotating the first strand, ensuring that the $CcdA_2$ DNA binding domains are still located in the major groove of the DNA (Figure 3C).

$CcdA_2$ has low affinity and specificity for single operator sites

In order to further understand how the observed structures confer operator specificity and affinity in a cellular context, we studied the interaction of $CcdA_2$ and $CcdB_2$ with the operator using EMSA and ITC. The F plasmid *ccdAB* operator consists of a rather long 113 bp stretch of DNA that contains at least eight binding sites for the antitoxin $CcdA_2$ (28). At the center of this operator are three short GTATAC palindromes, one perfect and two imperfect ones (20) (Figure 4A). It has been proposed that these three palindromes serve as nucleation sites for the binding of $CcdA_2$ and $CcdB_2$ to the complete operator (28) and thus that $CcdA_2$ specifically recognizes this palindrome. To test this hypothesis, we used the SwitchSENSE technology to measure the interaction of $CcdA_2$ with all 64 possible 6 bp palindrome sequences. Surprisingly, the results indicate that $CcdA_2$ does not discriminate significantly between the different sequences (Supplementary Figure S10). Moreover, several $CcdA_2$ dimers appear to bind simultaneously to the nanolever DNA used in the experiment, indicating poor specificity.

EMSA experiments carried out in the presence of an excess of non-specific competitor DNA provide further indications that $CcdA_2$ has a low affinity and specificity for DNA. The affinity for a 42 bp sequence containing a single GTATAC palindrome (Figure 4B and C, Supplementary Table S4) is only slightly higher than the one for the random sequence of the same length (Figure 4B and C, Supplementary Table S4). As more palindromes (binding sites) are inserted into the fragment, we observe an increase in the apparent affinity, which becomes highest for the full 113 bp operator sequence (Figure 4B and C, Supplementary Table S4). These experiments show that some sequence specificity is associated with the binding of $CcdA_2$ to the operator.

$CcdB_2$ increases both affinity and specificity of $CcdA_2$ for its operator

The affinity of $CcdA_2$ for DNA increases significantly in the presence of $CcdB_2$ (Figure 5A). This increase in affinity is observed for both short and full-length operator fragments and depends on the ratio of $CcdB_2$ to $CcdA_2$, in agreement with the presence of conditional cooperativity (12). For both the 42 bp fragment containing three binding sites as well as the full length operator, a clear increase in the affinity of $CcdA_2$ for the DNA is observed as long as the $CcdB_2$:$CcdA_2$ ratio remains below 1. For the full length operator, the switch from repression to non-repression occurs abruptly at the moment the $CcdB_2$:$CcdA_2$ ratio exceeds 1.

Moreover, $CcdB_2$ enhances the specificity of $CcdA_2$ for its cognate DNA. In the presence of the toxin, a clear band shift is observed for the DNA fragment with three central binding sites at 1.5 μM $CcdA_2$ and 0.75 μM $CcdB_2$ (Figure 5B). On the other hand, no binding is observed to a random DNA fragment of the same length even at three times higher concentrations (Figure 5C). Thus, $CcdB_2$ increases the affinity of $CcdA_2$ for a native promoter sequence (with specific 5′-GTATAC-3′ palindromes) more than it does for a non-specific random sequence.

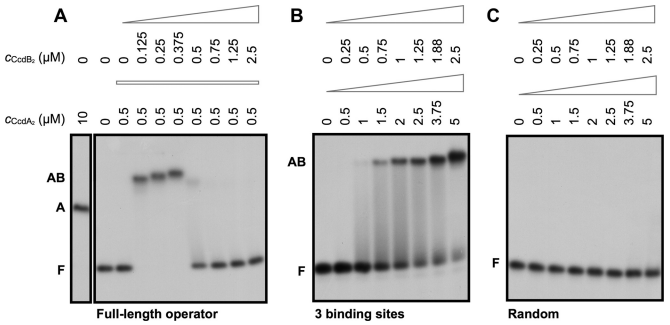

Figure 5. The toxin $CcdB_2$ increases the affinity and specificity of the antitoxin $CcdA_2$ for the DNA at low toxin:antitoxin ratios. Autoradiographs of EMSA analyses of $CcdA_2$ and $CcdB_2$ binding to fragments of the *ccdAB* operator. The concentrations of $CcdA_2$ and $CcdB_2$ are indicated above the lanes. The positions of free DNA (marked as F), DNA bound by $CcdA_2$ (marked as A) and DNA bound by $CcdA_2$ and $CcdB_2$ (marked as AB) are indicated next to the lanes. (**A**) The $CcdB_2$ concentration is varied in the presence of a constant concentration of $CcdA_2$. (**B** and **C**) The concentration of $CcdA_2$ and $CcdB_2$ is varied while maintaining a constant toxin:antitoxin ratio.

Coordinated binding of multiple $CcdA_2$ domains ensures a high affinity for the operator DNA

Next, we used ITC to investigate the thermodynamics governing the regulation of *ccdAB* expression. For practical reasons, the operator fragment containing three central binding sites for $CcdA_2$ was used. A model that considers $(CcdA_2\text{-}CcdB_2)_3$:DNA, a single chain of three $CcdA_2$-$CcdB_2$ units bound to the DNA, as the only repressing species was fitted globally to the ITC data (60,65) (see Materials and Methods). This simple model agrees well with the whole data set and suggests that the formation of the repressing complex is highly favorable (Figure 6, Supplementary Figure S1, Supplementary Table S1). Assuming that pairwise binding free energies are approximately additive (see the Supplementary Data for a more rigorous discussion), most of the stability of this complex (80%) comes from the formation of the $(CcdA_2\text{-}CcdB_2)_3$ alternating chain. The remainder can be ascribed to the binding of three $CcdA_2$ dimers to three binding sites on the DNA (Figure 6B, ΔG°). This gives a free energy contribution of only −5.4 kcal/mol per binding site, which corresponds to a K_d value in the high micromolar range ($K_d = e^{\Delta G^\circ / RT}$). However, by coupling the three $CcdA_2$ dimers together and forcing them to bind to the DNA simultaneously, their binding free energies combine. As the K_d values multiply, this results in a high affinity of $(CcdA_2\text{-}CcdB_2)_3$ for DNA. The entropic cost of constraining multiple $CcdA_2$ units into the alternating $CcdA_2$-$CcdB_2$ chain ($-T\Delta S^\circ >> 0$) is paid for by the otherwise highly favorable $CcdA_2$-$CcdB_2$ interaction energy ($\Delta H^\circ << 0$) and desolvation of hydrophobic surfaces ($\Delta C_p{}^\circ < 0$).

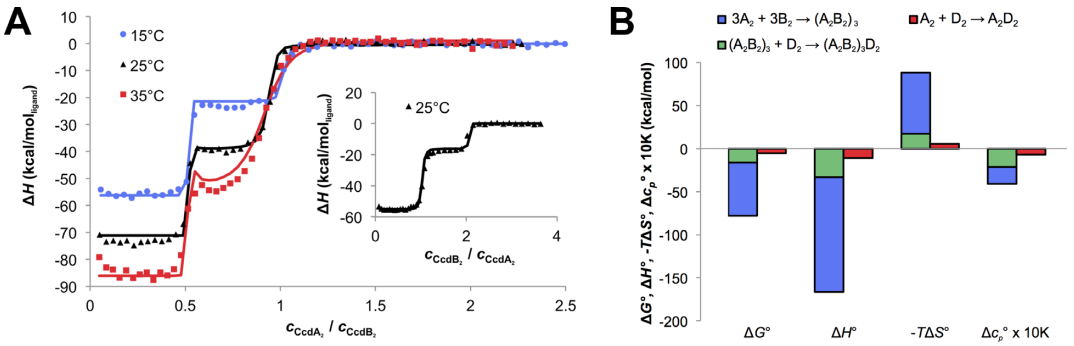

Figure 6. Coupling multiple $CcdA_2$ antitoxins together is necessary to obtain a high affinity for the operator DNA. (**A**) Titrations of $CcdA_2$ into a $CcdB_2$:DNA 3:1 mixture. Note that each DNA molecule (D_2) has three binding sites for $CcdA_2$ (A_2). Inset: titration of $CcdB_2$ (B_2) into a $CcdA_2$:DNA 3:1 mixture. Symbols represent experimental data while lines of the same color represent the best fit of the global thermodynamic model (see Supplementary Figure S1). (**B**) Thermodynamic fingerprint of the $CcdA_2$-$CcdB_2$-DNA interactions: thermodynamic parameters for the assembly of the repressing complex on a DNA fragment containing three binding sites (blue and green) compared to the binding of $CcdA_2$ alone to one binding site on the DNA fragment (red; see also Supplementary Table S1).

The transcriptional autoregulation in the *ccdAB* operon is strongly ratio-dependent

The experimentally obtained thermodynamic parameters allow us to rigorously calculate the concentrations of each molecular species in the *ccdAB* system under a wide range of conditions. A schematic overview of the interactions in the toxin–antitoxin module, depending on the relative amounts of toxin and antitoxin, is shown in Figure 7A. More quantitatively, we calculated the regulatory phase space accessible to the *ccdAB* system (with an operator containing three binding sites for $CcdA_2$) at given total concentrations of the antitoxin $CcdA_2$ and the toxin $CcdB_2$. The state of the operator (free or repressed) strongly depends on the ratio of the total $CcdA_2$ and $CcdB_2$ concentrations, with a characteristic diagonal division of the phase space, which is a hallmark of ratio-dependent gene regulation (66) (Figure 7B). The diagonal separates the area with the free operator (at toxin:antitoxin ratios above two) from the area with the repressed operator (at toxin:antitoxin ratios below two). Additionally, below a threshold toxin concentration the operator is always in the unbound state, allowing new antitoxin and toxin to be produced.

The ratio-dependent switching can then be inferred from one-dimensional sections in the phase diagram, where at a fixed antitoxin concentration we increase the concentration of the toxin (this corresponds to the setup of the EMSA experiments in Figure 5A). When $CcdA_2$ is in excess and at least some $CcdB_2$ is present to bridge the antitoxin, repressor complexes will form on the *ccdAB* promoter (Figure 7C). Such complexes are stabilized by both high and low affinity interactions and the interaction with the operator (Figure 6B). However, upon increase of the $CcdB_2$ concentration, the more stable, non-repressing heterohexameric complexes form, breaking up the $CcdA_2$-$CcdB_2$ alternating chains and lifting repression. Although the switch to the heterohexameric complex is accompanied by the loss of favorable interactions with the operator and low-affinity $CcdA_2$-$CcdB_2$ interactions in the alternating chain, this is compensated by the formation of high-affinity interactions between $CcdA_2$ and the additional $CcdB_2$. Thus, switching between the repressing and the non-repressing complex is defined by the relative difference between the high and low affinity $CcdA_2$-$CcdB_2$ binding constants. The observed difference is six orders of magnitude (Supplementary Table S1), which is consistent with the optimal response predicted by our simulations (Supplementary Figure S3C and D).

A high multiplicity of operator binding sites ensures efficient repression in the presence of non-specific DNA

Thermodynamic modeling of the *ccdAB* system sheds light on how multiple binding sites affect the regulatory mechanism. If only one binding site on the operator is considered, the system does not exhibit repression at physiological concentrations due to the low DNA binding affinity of $CcdA_2$ (Figure 7D). An increasing number of binding sites leads to stronger repression, eventually resulting in a digital-like switch for a model with eight binding sites on the operator (Figure 7E, Supplementary Figure S3A). Importantly, simulated systems with higher affinity lack the ratio-sensitive switch, indicating that the low affinity of $CcdA_2$ for an individual binding site is crucial for the functionality of the mechanism (Supplementary Figure S3B). Low affinity for the operator ensures that only multivalent chain complexes of $(CcdA_2{:}CcdB_2)_n$ are active repressors while heterohexamers and isolated $CcdA_2$ bind too weakly to be effective.

Given the low specificity of a single $CcdA_2$ antitoxin for a binding site on the operator, we asked how functional repression can be achieved in the presence of non-specific DNA. The affinity constant for the non-specific DNA was assumed to be 1/3 of that for the specific DNA. Several values of the affinity constant for the non-specific DNA were tested and good agreement with EMSA results was found when the estimated value for the non-specific DNA was 1/3 of that for the specific one. The model of the system based on the ITC experiments that takes into account only $(CcdA_2$-$CcdB_2)_8$ and $CcdB_2$-$CcdA_2$-$CcdB_2$ as repressing and non-repressing complexes reproduces the EMSA results on the full length operator in the presence of non-specific DNA to a certain extent, in particular the ratio-dependent on-off behavior (Supplementary Figure S2C). However, agreement with the EMSA is significantly improved using an extended model, where all possible ($CcdA_2$-

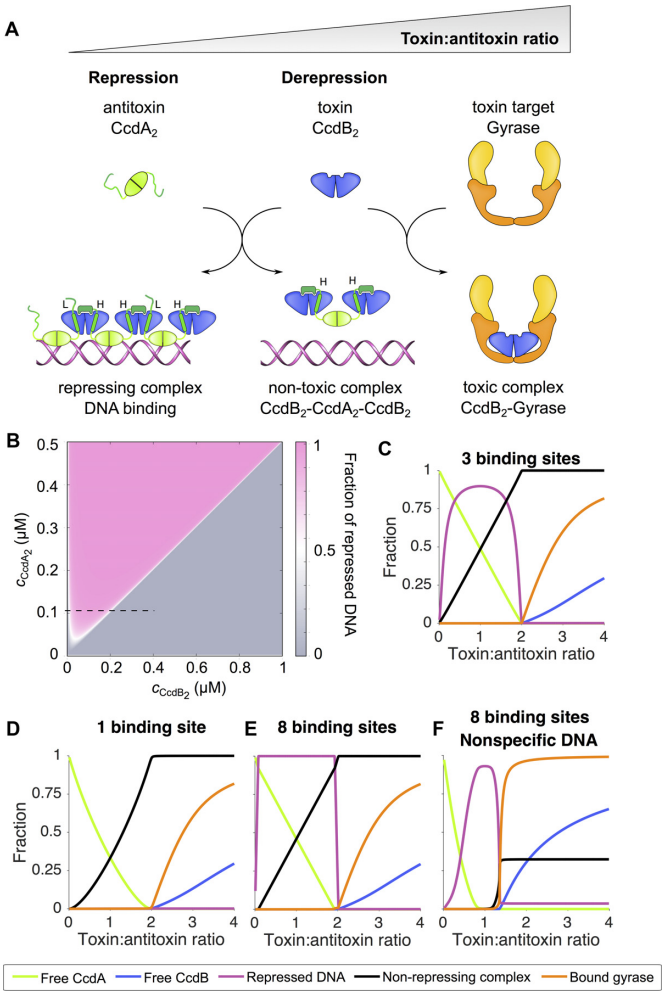

Figure 7. Multiple coupled low-affinity binding sites on the operator ensure a tight ratio-dependent transcriptional regulation of the *ccdAB* operon. (**A**) Schematic overview of the regulation of the *ccdAB* operon. The toxin:antitoxin ratio increases from left to right. (**B**) Heat plot showing the fraction of repressed operator DNA as a function of the dimer concentrations of $CcdA_2$ and $CcdB_2$. (**C**) Horizontal cross-section of the phase diagram as indicated by the dotted line on the heat plot. The curves represent the fraction of free $CcdA_2$ relative to the total amount of $CcdA_2$ (green), the fraction of free $CcdB_2$ relative to the total amount of $CcdB_2$ (blue), the fraction of bound DNA relative to the total amount of DNA (magenta), the fraction of non-repressing complex $CcdB_2$-$CcdA_2$-$CcdB_2$ relative to the total amount of $CcdA_2$ (black) and the fraction of bound gyrase relative to the total amount of gyrase (orange). (**D–F**) Simulations of the regulation of the *ccdAB* operon demonstrate the effect of multiple binding sites and the effects of non-specific DNA. Panels C–E show simulations performed with the simple model in the absence of non-specific DNA, panel F shows the simulation with the extended model in the presence of non-specific DNA. Model descriptions are given in Materials and Methods. All calculations are performed at 25°C.

$(CcdB_2)_n$ chain complexes on the operator and on non-specific DNA are considered (Figure 7F). Particularly, this extended model correctly predicts that in the presence of non-specific DNA the de-repression occurs at lower $CcdB_2$ to $CcdA_2$ ratios (but still above one), as observed in EMSA (Figure 5A). This stems from the ratio-dependence of the stoichiometry of the $(CcdA_2\text{-}CcdB_2)_n$ repressor complex: at low $CcdB_2$:$CcdA_2$ ratios, shorter chains with lower specificity are favored, which gradually grow to the more specific $(CcdA_2\text{-}CcdB_2)_8$ complex at equimolar ratios, in accordance with gradual supershifting of the repressor complex observed in EMSA (Supplementary Figure S2E, Figure 5A). At $CcdB_2$:$CcdA_2$ ratios above 1, the species distribution changes rapidly and repression is relieved due to lack of specific high stoichiometry $(CcdA_2\text{-}CcdB_2)_n$ complexes and concomitant formation of the non-repressing $CcdB_2$-$CcdA_2$-$CcdB_2$ complex. Thus, in contrast to what intuitively may be expected, a relatively weak specificity may not be detrimental but can be functionally relevant.

DISCUSSION

Conditional cooperativity is a central mechanism in the transcriptional regulation of several type II toxin–antitoxin modules, involving repression at low toxin:antitoxin ratios and derepression at high toxin:antitoxin ratios. Although the *ccdAB* operon on the F plasmid of *E. coli* was the first TA module found to be regulated via conditional cooperativity (26), the underlying molecular mechanisms are not yet fully understood.

We elucidated the autoregulation of the *ccdAB* module by determining the structures of the full repressing complex and the non-repressing $CcdB_2$-$CcdA_2$-$CcdB_2$ heterohexamer and by a thermodynamic characterization of all known toxin–antitoxin–DNA interactions within the system. Based on this analysis, we also propose a quantitative model that allows us to describe and simulate the functional behavior of the entire system. The main hallmark of the *ccdAB* autoregulation is its dependence on the ratio of two proteins, which is manifested as the diagonal division of the regulatory phase space (Figure 7B).

The $CcdB_2$-$CcdA_2$-$CcdB_2$ heterohexamer has a V-shaped architecture, with the DNA-binding domain of the antitoxin located in the center, and two toxins at the extremities. This general lay-out has also been found in several other TA modules, such as *E. coli relBE* (67), bacteriophage P1 *phd/doc* (68), *E. coli mqsRA* (69) and *E. coli* and *Bacillus subtilis mazEF* (70,71). The limited dynamics observed in the $CcdB_2$-$CcdA_2$-$CcdB_2$ heterohexamer may serve to allow the $CcdA_2$-$CcdB_2$ dimers to accommodate operator binding sites with slightly different angles and distances between them without interrupting the repressing complex. This repressing complex has an unusual and hitherto unobserved architecture, consisting of an elongated chain of alternating DNA-bound $CcdA_2$ antitoxins bridged by $CcdB_2$ toxins. The ratio-dependent regulation can be entirely explained based on the increase of the affinity induced by the multiplicity of binding sites on the operator, in contrast to the *phd/doc* operon where cooperative and allosteric effects play a key role (22,23). This difference might be related to the structure of the operators – the *ccdAB* promoter/operator region contains eight putative antitoxin binding sites (28), compared to only two in *phd/doc* (72).

We found that the 3D map for the thin filaments cannot be explained by the presence of only one strand of alternating toxin and antitoxin dimers. However, as we discuss below, the second spiral detected with EM is most likely a result of a concentration-dependent effect observed only in the absence of an excess of non-specific DNA that would

act as a sink for $CcdA_2$-$CcdB_2$ chain complexes. To clarify this issue, we performed simulations in which the formation of the second spiral is allowed via sequential binding of the $CcdA_2$-$CcdB_2$ chain to the pre-existing single spiral $CcdA_2$-$CcdB_2$-operator complex, using the 'simple model' in which only the formation of $CcdA_2$-$CcdB_2$ chains that cover the whole operator fragment is allowed. We find that at the concentrations used in EM measurements, the second spiral is always bound to the DNA fragment (the fraction of the operator bound by two spirals is more than 99% relative to the total operator DNA), while at the conditions of the ITC measurements, the fraction of the operator fragment with two bound $CcdA_2$-$CcdB_2$ chains is negligibly small.

By contrast, when an excess of non-specific DNA is included in these simulations, the fraction of the complex with a second spiral is less than 1% even at the highest protein concentrations used in the EM measurements. Based on these results, we conclude that the formation of the second spiral is strongly concentration dependent, but more significantly, that the presence of an excess of non-specific competitor DNA abolishes the formation of the second spiral. Therefore, we believe that *in vivo,* where the concentration of non-specific DNA is significant, the formation of the second spiral on the operator is very unlikely. Generally, the binding of the second spiral does not affect the ratio-dependent regulation, which was found to be independent of the total $CcdA_2$ and $CcdB_2$ concentrations in the 0.1–10 μM range. Since the *in vivo* toxin and antitoxin concentrations are very likely in this concentration range (25,73), we believe that the regulatory properties predicted by the model (presented in the phase diagram) correspond well with the situation in the cellular environment.

The influence of the non-specific competitor DNA on the operator binding by $CcdA_2$ and $CcdB_2$ is also clearly illustrated by the DNase I footprinting experiment performed by Dao-Thi *et al.* (28). While the region of DNA bound by $CcdA_2$ and $CcdB_2$ is larger than the actual *ccdAB* operator in our EM measurements, the DNase I footprint, performed in the presence of a large excess of non-specific competitor DNA, only includes eight well-defined binding sites in the 113 bp region identified by Tam and Kline (27).

The most unusual and intriguing aspect of the *ccdAB* autoregulation is the low affinity and specificity of $CcdA_2$ for its binding sites on the operator. The low operator affinity of $CcdA_2$ prevents repression in the absence of $CcdB_2$. In the presence of the toxin, $CcdB_2$ dimers will link $CcdA_2$ dimers together to form multivalent chains where the weak affinities of individual $CcdA_2$ molecules are multiplied to provide a strong avidity. The small difference between affinities for cognate and non-cognate binding sites is similarly enlarged, which explains why DNA binding is more sequence-specific in the presence of $CcdB_2$. This effect breaks down at higher $CcdB_2$:$CcdA_2$ ratios when $CcdB_2$-$CcdA_2$-$CcdB_2$ complexes start to form. With only one DNA binding domain per complex, they again bind the DNA weakly, with the additional limitation that adjacent binding sites cannot be occupied due to steric clashes between $CcdB_2$ dimers. This ensures that repression is lifted once the toxin:antitoxin ratio becomes too high. To our knowledge, this mechanism is unique in transcription regulation. Even in the *mazEF* family, which is related to *ccdAB* in terms of toxin structure and dynamics as well as in the way by which the antitoxin interacts with the toxin and regulates its activity (74–76), no extended operator or poor discrimination of DNA sequences has been reported. The well-studied *mazEF* homologue *kis/kid* on plasmid R1 was indeed shown *in vitro* to form extended alternating chains of toxin and antitoxin (77), but the operator complex is limited to a Kid_2-Kis_2-Kid_2-Kis_2 complex binding to a piece of operator DNA with two binding sites (78).

The *ccdAB* system behaves non-intuitively in terms of specificity requirements. One would expect that poor discrimination of the correct binding sites on the operator from non-specific chromosomal DNA should be detrimental for the cell, both due to poorly controlled repression of the *ccdAB* operon (leading to $CcdB_2$-based toxicity) and to uncontrolled random repression of genes, disturbing cellular physiology. Yet our model clearly shows that a tight repression can be established by the coupled binding of several antitoxins bridged by $CcdB_2$ toxins to the binding sites on the operator. Furthermore, the fact that specificity for the operator increases with the length of the $(CcdA_2\text{-}CcdB_2)_n$ chain prevents random patches of chromosomal DNA from being covered with these high-affinity complexes, and therefore $CcdA_2$ and $CcdB_2$ are unlikely to deregulate normal gene expression in *E. coli*. Altogether, the *ccdAB* system provides a unique and non-intuitive solution to a complex problem of gene regulation that depends on the multiplicity of antitoxin binding sites on the operator to generate both affinity and specificity.

ACCESSION NUMBERS

The SAXS Scattering data and model for $CcdB_2$-$CcdA_2$-$CcdB_2$ has been deposited to SASBDB (ID SASDBA9). The 3D reconstructions based on the EM data have been deposited to EMDB (ID EMD-3568 for the negative stain data set of the thin filaments and ID EMD-3569 for the cryo-EM data set of the thick filaments).

SUPPLEMENTARY DATA

Supplementary Data are available at NAR Online.

ACKNOWLEDGEMENTS

The authors thank the beamline staff from synchrotron Soleil – Swing for the technical support. The authors further thank Sarah Haesaerts for protein purification and Mike Sleutel for fruitful discussions.

FUNDING

Vlaams Interuniversitair Instituut voor Biotechnologie [VIB6; Q1-2011 to R.L.]; Fonds voor Wetenschappelijk Onderzoek Vlaanderen [G.0135.15N to R.L. and R.E., G0C1213N, G.0878.12N; G.0090.11N to R.L., FWOTM637 to A.V.]; Onderzoeksraad of the Vrije Universiteit Brussel [OZR2232 to S.H., SPR13 to R.L.]; European Community's Seventh Framework Program (FP7/2007-2013) under BioStruct-X [projects 1673 and 6131 to R.L.]; Hercules Foundation [UABR/11/012 to

R.L.]; Slovenian Research Agency [P1–0201 and J1-5448 to J.L.]; Bundesministerium für Bildung und Forschung (BMBF) [GO-Bio program 031A240 to T.W.]. Funding for open access charge: Fonds voor Wetenschappelijk Onderzoek Vlaanderen [G.0135.15N].
Conflict of interest statement. None declared.

REFERENCES

1. Lewis,K. (2010) Persister cells. *Annu. Rev. Microbiol.*, **64**, 357–372.
2. Lewis,K. (2007) Persister cells, dormancy and infectious disease. *Nat. Rev. Microbiol.*, **5**, 48–56.
3. Bigger,J.W. (1944) Treatment of staphylococcal infections with penicillin. *Lancet*, **244**, 497–500.
4. Keren,I., Kaldalu,N., Spoering,A., Wang,Y. and Lewis,K. (2004) Persister cells and tolerance to antimicrobials. *FEMS Microbiol. Lett.*, **230**, 13–18.
5. Lewis,K. (2008) Multidrug tolerance of biofilms and persister cells. *Curr. Top. Microbiol. Immunol.*, **322**, 107–131.
6. Fauvart,M., De Groote,V.N. and Michiels,J. (2011) Role of persister cells in chronic infections: clinical relevance and perspectives on anti-persister therapies. *J. Med. Microbiol.*, **60**, 699–709.
7. Hayes,F. and Van Melderen,L. (2011) Toxins-antitoxins: diversity, evolution and function. *Crit. Rev. Biochem. Mol. Biol.*, **46**, 386–408.
8. Gerdes,K., Christensen,S.K. and Lobner-Olesen,A. (2005) Prokaryotic toxin-antitoxin stress response loci. *Nat. Rev. Microbiol.*, **3**, 371–382.
9. Maisonneuve,E., Shakespeare,L., Jørgensen,M.G. and Gerdes,K. (2011) Bacterial persistence by RNA endonucleases. *Proc. Natl. Acad. Sci. U.S.A.*, **108**, 13206–13211.
10. Dörr,T., Vulić,M. and Lewis,K. (2010) Ciprofloxacin causes persister formation by inducing the TisB toxin in *Escherichia coli*. *PLoS Biol.*, **8**, e1000317.
11. Christensen-Dalsgaard,M., Jørgensen,M.G. and Gerdes,K. (2010) Three new RelE-homologous mRNA interferases of *Escherichia coli* differentially induced by environmental stresses. *Mol. Microbiol.*, **75**, 333–348.
12. Miki,T., Yoshioka,K. and Horiuchi,T. (1984) Control of cell-division by sex factor F in *Escherichia coli*. 1. The 42.84-43.6 F segment couples cell-division of the host bacteria with replication of F plasmid DNA. *J. Mol. Biol.*, **174**, 605–625.
13. Bernard,P. and Couturier,M. (1992) Cell killing by the F plasmid CcdB protein involves poisoning of DNA-topoisomerase II complexes. *J. Mol. Biol.*, **226**, 735–745.
14. Dao-Thi,M.-H., Van Melderen,L., De Genst,E., Afif,H., Buts,L., Wyns,L. and Loris,R. (2005) Molecular basis of gyrase poisoning by the addiction toxin CcdB. *J. Mol. Biol.*, **348**, 1091–1102.
15. Critchlow,S.E., O'Dea,M.H., Howells,A.J., Couturier,M., Gellert,M. and Maxwell,A. (1997) The interaction of the F plasmid killer protein, CcdB, with DNA gyrase: induction of DNA cleavage and blocking of transcription. *J. Mol. Biol.*, **273**, 826–839.
16. Bernard,P., Kézdy,K.E., Van Melderen,L., Steyaert,J., Wyns,L., Pato,M.L., Higgins,P.N. and Couturier,M. (1993) The F plasmid CcdB protein induced efficient ATP-dependent DNA cleavage by gyrase. *J. Mol. Biol.*, **234**, 534–541.
17. Maki,S., Takiguchi,S., Horiuchi,T., Sekimizu,K. and Miki,T. (1996) Partner switching mechanisms in inactivation and rejuvenation of *Escherichia coli* DNA gyrase by F plasmid proteins LetD (CcdB) and LetA (CcdA). *J. Mol. Biol.*, **256**, 473–482.
18. De Jonge,N., Garcia-Pino,A., Buts,L., Haesaerts,S., Charlier,D., Zangger,K., Wyns,L., De Greve,H. and Loris,R. (2009) Rejuvenation of CcdB-poisoned gyrase by an intrinsically disordered protein domain. *Mol. Cell*, **35**, 154–163.
19. Tripathi,A., Dewan,P.C., Barua,B. and Varadarajan,R. (2012) Additional role for the *ccd* operon of F-plasmid as a transmissible persistence factor. *Proc. Natl. Acad. Sci. U.S.A.*, **109**, 12497–12502.
20. Madl,T., Van Melderen,L., Mine,N., Respondek,M., Oberer,M., Keller,W., Khatai,L. and Zangger,K. (2006) Structural basis for nucleic acid and toxin recognition of the bacterial antitoxin CcdA. *J. Mol. Biol.*, **364**, 170–185.
21. Van Melderen,L., Bernard,P. and Couturier,M. (1994) Lon-dependent proteolysis of CcdA is the key control for activation of CcdB in piasmid-free segregant bacteria. *Mol. Microbiol.*, **11**, 1151–1157.
22. Garcia-Pino,A., Balasubramanian,S., Wyns,L., Gazit,E., De Greve,H., Magnuson,R.D., Charlier,D., van Nuland,N.A. and Loris,R. (2010) Allostery and intrinsic disorder mediate transcription regulation by conditional cooperativity. *Cell*, **142**, 101–111.
23. Garcia-Pino,A., De Gieter,S., Talavera,A., De Greve,H., Efremov,R.G. and Loris,R. (2016) An intrinsically disordered entropic switch determines allostery in Phd-Doc regulation. *Nat. Chem. Biol.*, **12**, 490–496.
24. Overgaard,M., Borch,J., Jorgensen,M.G. and Gerdes,K. (2008) Messenger RNA interferase RelE controls *relBE* transcription by conditional cooperativity. *Mol. Microbiol.*, **69**, 841–857.
25. Overgaard,M., Borch,J. and Gerdes,K. (2009) RelB and RelE of *Escherichia coli* form a tight complex that represses transcription via the ribbon-helix-helix motif in RelB. *J. Mol. Biol.*, **394**, 183–196.
26. Afif,H., Allali,N., Couturier,M. and Van Melderen,L. (2001) The ratio between CcdA and CcdB modulates the transcriptional repression of the *ccd* poison-antidote system. *Mol. Microbiol.*, **41**, 73–82.
27. Tam,J.E. and Kline,B.C. (1989) Control of the *ccd* operon in plasmid F. *J. Bacteriol.*, **171**, 2353–2360.
28. Dao-Thi,M.-H., Charlier,D., Loris,R., Maes,D., Messens,J., Wyns,L. and Backmann,J. (2002) Intricate interactions within the *ccd* plasmid addiction system. *J. Biol. Chem.*, **277**, 3733–3742.
29. Loris,R. and Garcia-Pino,A. (2014) Disorder and dynamics-based regulatory mechanisms in toxin-antitoxin modules. *Chem. Rev.*, **114**, 6933–6947.
30. Flock,T., Weatheritt,R.J., Latysheva,N.S. and Babu,M.M. (2014) Controlling entropy to tune the functions of intrinsically disordered regions. *Curr. Opin. Struct. Biol.*, **26C**, 62–72.
31. Crothers,D.M. and Metzger,H. (1972) The influence of polyvalency on the binding properties of antibodies. *Immunochemistry*, **9**, 341–357.
32. Hornickt,C.L. and Karush,F. (1972) Antibody affinity - III the role of multivalence. *Immunochemistry*, **9**, 325–330.
33. Brewer,C.F., Miceli,M.C. and Baum,L.G. (2002) Clusters, bundles, arrays and lattices: Novel mechanisms for lectin-saccharide-mediated cellular interactions. *Curr. Opin. Struct. Biol.*, **12**, 616–623.
34. Lasky,L.A. (1995) Selectin-carbohydrate interactions and the initiation of the inflammatory response. *Annu. Rev. Biochem.*, **64**, 113–139.
35. Holmskov,U., Thiel,S. and Jensenius,J.C. (2003) Collectins and ficolins: Humoral lectins of the innate immune defense. *Annu. Rev. Immunol.*, **21**, 547–578.
36. Turner,M.W. (2004) The role of mannose-binding lectin in health and disease. *Mol. Immunol.*, **62**, 4–9.
37. Dao-Thi,M.-H., Van Melderen,L., De Genst,E., Buts,L., Ranquin,A., Wyns,L. and Loris,R. (2004) Crystallization of CcdB in complex with a GyrA fragment. *Acta Crystallogr. D Biol. Crystallogr.*, **60**, 1132–1134.
38. Van Melderen,L., Dao-Thi,M.H., Lecchi,P., Gottesman,S., Couturier,M. and Maurizi,M.R. (1996) ATP-dependent degradation of CcdA by Lon protease - Effects of secondary structure and heterologous subunit interactions. *J. Biol. Chem.*, **271**, 27730–27738.
39. David,G. and Pérez,J. (2009) Combined sampler robot and high-performance liquid chromatography: a fully automated system for biological small-angle X-ray scattering experiments at the Synchrotron SOLEIL SWING beamline. *J. Appl. Crystallogr.*, **42**, 892–900.
40. Shkumatov,A.V and Strelkov,S.V (2015) DATASW, a tool for HPLC-SAXS data analysis. *Acta Crystallogr. D Biol. Crystallogr.*, **71**, 1347–1350.
41. Petoukhov,M.V., Franke,D., Shkumatov,A.V., Tria,G., Kikhney,A.G., Gajda,M., Gorba,C., Mertens,H.D.T., Konarev,P.V. and Svergun,D.I. (2012) New developments in the ATSAS program package for small-angle scattering data analysis. *J. Appl. Crystallogr.*, **45**, 342–350.
42. Svergun,D.I. (1992) Determination of the regularization parameter in indirect-transform. *J. Appl. Crystallogr.*, **25**, 495–503.
43. Franke,D. and Svergun,D.I. (2009) *DAMMIF*, a program for rapid *ab-initio* shape determination in small-angle scattering. *J. Appl. Crystallogr.*, **42**, 342–346.

44. Volkov,V.V. and Svergun,D.I. (2003) Uniqueness of *ab initio* shape determination in small-angle scattering. *J. Appl. Crystallogr.*, **36**, 860–864.
45. Schneidman-Duhovny,D., Hammel,M. and Sali,A. (2010) FoXS: a web server for rapid computation and fitting of SAXS profiles. *Nucleic Acids Res.*, **38**, W540–W544.
46. Weinkam,P., Pons,J. and Sali,A. (2012) Structure-based model of allostery predicts coupling between distant sites. *Proc. Natl. Acad. Sci. U.S.A.*, **109**, 4875–4880.
47. Svergun,D.I., Barberato,C. and Koch,M.H.J. (1995) CRYSOL – a program to evaluate X-ray solution scattering of biological macromolecules from atomic coordinates. *J. Appl. Crystallogr.*, **28**, 768–773.
48. Miller,J.H. (1992) A short course in bacterial genetics: a laboratory manual and handbook for *Escherichia coli* and related bacteria. Cold Spring Harbor Laboratory Press, NY.
49. Tang,G., Peng,L., Baldwin,P.R., Mann,D.S., Jiang,W., Rees,I. and Ludtke,S.J. (2007) EMAN2: an extensible image processing suite for electron microscopy. *J. Struct. Biol.*, **157**, 38–46.
50. Behrmann,E., Tao,G., Stokes,D.L., Egelman,E.H., Raunser,S. and Penczek,P.A (2012) Real-space processing of helical filaments in SPARX. *J. Struct. Biol.*, **177**, 302–313.
51. Finch,J.T. (1972) The hand of the helix of tobacco virus. *J. Mol. Biol.*, **66**, 291–294.
52. van Dijk,M. and Bonvin,A.M.J.J. (2009) 3D-DART: A DNA structure modelling server. *Nucleic Acids Res.*, **37**, W235–W239.
53. Emsley,P., Lohkamp,B., Scott,W.G. and Cowtan,K. (2010) Features and development of Coot. *Acta Crystallogr. D Biol. Crystallogr.*, **66**, 486–501.
54. Pettersen,E.F., Goddard,T.D., Huang,C.C., Couch,G.S., Greenblatt,D.M., Meng,E.C. and Ferrin,T.E. (2004) UCSF Chimera - a visualization system for exploratory research and analysis. *J. Comput. Chem.*, **25**, 1605–1612.
55. Langer,A., Hampel,P.A, Kaiser,W., Knezevic,J., Welte,T., Villa,V., Maruyama,M., Svejda,M., Jähner,S., Fischer,F. *et al.* (2013) Protein analysis by time-resolved measurements with an electro-switchable DNA chip. *Nat. Commun.*, **4**, 2099–2107.
56. Pace,C.N., Vajdos,F., Fee,L., Grimsley,G. and Gray,T. (1995) How to measure and predict the molar absorption coefficient of a protein. *Protein Sci.*, **4**, 2411–2423.
57. Cantor,C.R., Warshaw,M.M. and Shapiro,H. (1970) Oligonucleotide interactions. III. Circular dichroism studies of the conformation of deoxyoligonucleolides. *Biopolymers*, **9**, 1059–1077.
58. Huang,C.Y. (1982) Determination of binding stoichiometry by the continuous variation method: the Job plot. *Methods Enzymol.*, **87**, 509–525.
59. Drobnak,I., De Jonge,N., Haesaerts,S., Vesnaver,G., Loris,R. and Lah,J. (2013) Energetic basis of uncoupling folding from binding for an intrinsically disordered protein. *J. Am. Chem. Soc.*, **135**, 1288–1294.
60. Drobnak,I., Vesnaver,G. and Lah,J. (2010) Model-based thermodynamic analysis of reversible unfolding processes. *J. Phys. Chem. B*, **114**, 8713–8722.
61. Press,W.H., Teukolsky,S.A., Vetterling,W.T. and Flannery,B.P. (2002) Numerical Recipes in C++: the art of scientific computing. Cambridge University Press, Cambridge .
62. Powell,M.J.D. (1970) A hybrid method for nonlinear equations. In *Numerical methods for nonlinear equations*. Gordon and Breach, London, pp. 87–114.
63. Moré,J.J., Garbow,B.S. and Hillstrom,K.E. (1980) User guide for MINPACK-1. *Argonne National Laboratory Report ANL-80-74*, Argonne.
64. von Hippel,P.H., Revzin,A., Gross,C. A and Wang,A.C. (1974) Non-specific DNA binding of genome regulating proteins as a biological control mechanism: I. The *lac* operon: equilibrium aspects. *Proc. Natl. Acad. Sci. U.S.A.*, **71**, 4808–4812.
65. Simic,M., De Jonge,N., Loris,R., Vesnaver,G. and Lah,J. (2009) Driving forces of gyrase recognition by the addiction toxin CcdB. *J. Biol. Chem.*, **284**, 20002–20010.
66. Setty,Y., Mayo,A.E., Surette,M.G. and Alon,U. (2003) Detailed map of a cis-regulatory input function. *Proc. Natl. Acad. Sci. U.S.A.*, **100**, 7702–7707.
67. Bøggild,A., Sofos,N., Andersen,K.R., Feddersen,A., Easter,A.D., Passmore,L.A. and Brodersen,D.E. (2012) The crystal structure of the intact *E. coli* RelBE toxin-antitoxin complex provides the structural basis for conditional cooperativity. *Structure*, **20**, 1641–1648.
68. Arbing,M.A, Handelman,S.K., Kuzin,A.P., Verdon,G., Wang,C., Su,M., Rothenbacher,F.P., Abashidze,M., Liu,M., Hurley,J.M. *et al.* (2010) Crystal structures of Phd-Doc, HigA, and YeeU establish multiple evolutionary links between microbial growth-regulating toxin-antitoxin systems. *Structure*, **18**, 996–1010.
69. Brown,B.L., Grigoriu,S., Kim,Y., Arruda,J.M., Davenport,A., Wood,T.K., Peti,W. and Page,R. (2009) Three dimensional structure of the MqsR:MqsA complex: a novel TA pair comprised of a toxin homologous to RelE and an antitoxin with unique properties. *PLoS Pathog.*, **5**, e1000706.
70. Kamada,K., Hanaoka,F. and Burley,S.K. (2003) Crystal structure of the MazE/MazF complex: molecular bases of antidote-toxin recognition. *Mol. Cell*, **11**, 875–884.
71. Simanshu,D.K., Yamaguchi,Y., Park,J.H., Inouye,M. and Patel,D.J. (2013) Structural Basis of mRNA Recognition and Cleavage by Toxin MazF and Its Regulation by Antitoxin MazE in Bacillus subtilis. *Mol. Cell*, **52**, 447–458.
72. Gazit,E. and Sauer,R.T. (1999) Stability and DNA binding of the Phd protein of the phage P1 plasmid addiction system. *J. Biol. Chem.*, **274**, 2652–2657.
73. Li,G.-W., Burkhardt,D., Gross,C. and Weissman,J.S. (2014) Quantifying absolute protein synthesis rates reveals principles underlying allocation of cellular resources. *Cell*, **157**, 624–635.
74. Hargreaves,D., Santos-Sierra,S., Giraldo,R., Sabariegos-Jareño,R., de la Cueva-Méndez,G., Boelens,R., Díaz-Orejas,R. and Rafferty,J.B. (2002) Structural and functional analysis of the kid toxin protein from *E. coli* plasmid R1. *Structure*, **10**, 1425–1433.
75. Zorzini,V., Buts,L., Sleutel,M., Garcia-Pino,A., Talavera,A., Haesaerts,S., De Greve,H., Cheung,A., Van Nuland,N.A.J. and Loris,R. (2014) Structural and biophysical characterization of *Staphylococcus aureus* SaMazF shows conservation of functional dynamics. *Nucleic Acids Res.*, **42**, 6709–6725.
76. Zorzini,V., Mernik,A., Lah,J., Sterckx,Y.G.J., De Jonge,N., Garcia-Pino,A., De Greve,H., Versees,W. and Loris,R. (2016) Substrate recognition and activity regulation of the Escherichia coli mRNA endonuclease MazF. *J. Biol. Chem.*, **291**, 10950–10960.
77. Kamphuis,M.B., Monti,M.C., van den Heuvel,R.H.H., Santos-Sierra,S., Folkers,G.E., Lemonnier,M., Díaz-Orejas,R., Heck,A.J.R. and Boelens,R. (2008) Interactions between the toxin Kid of the bacterial *parD* system and the antitoxins Kis and MazE. *Proteins*, **70**, 311–319.
78. Monti,M.C., Hernández-Arriaga,A.M., Kamphuis,M.B., López-Villarejo,J., Heck,A.J.R., Boelens,R., Díaz-Orejas,R. and van den Heuvel,R.H.H. (2007) Interactions of Kid-Kis toxin-antitoxin complexes with the *parD* operator-promoter region of plasmid R1 are piloted by the Kis antitoxin and tuned by the stoichiometry of Kid-Kis oligomers. *Nucleic Acids Res.*, **35**, 1737–1749.